Letters

Analysis and Optimization of Current Dynamic Control in Induction Motor Field-Weakening Region

Xu Zhang, *Student Member, IEEE*, Bo Wang, *Member, IEEE*, Yong Yu, Jing Zhang, Jiaxin Dong, and Dianguo Xu, *Fellow, IEEE*

***Abstract*—The maximum-torque-output (MTO) trajectory can achieve optimal current distribution for induction motor (IM) field-weakening (FW) control. To provide the dynamic model for MTO, this letter proposes quantitative analysis of the current dynamic character in FW control. As the current vector moves along MTO trajectory, the current changing rate and voltage margin requirement are calculated to study the dynamic control objective and the realization condition of FW control. According to the summarized changing law of voltage margin requirement, the *d*-axis voltage margin priority approach is applied to the IM FW system for current dynamic optimization. The effectiveness of the studied method is verified through comparison experiments on an advanced RISC machine (ARM)-based 3.7-kW IM platform.**

***Index Terms*—Current dynamic control, field-weakening (FW) control, induction motor (IM), maximum torque output, quantitative analysis.**

I. Introduction

THE maximum-torque-output (MTO) trajectory is applied to induction motor (IM) field-weakening (FW) control to widen speed range and enhance load capacity [1], [2]. Under MTO trajectory, the inverter voltage can be fully used to offset the back electromotive force (EMF) of IM. However, the dynamic control performance of current regulator would be deteriorated due to the lack of voltage margin, leading to the current ripple.

In recent years, many approaches are proposed to improve the current performance of ac machines. In [3] and [4], the current ripple caused by overmodulation is suppressed by decreasing the dc-link voltage. The adjustable dc-link voltage is realized through the introduced dc-to-dc converter. Since the adjusted of hardware circuit is not easy to achieve in some applications, many other methods are presented for current performance optimization. To suppress the stator current harmonics, the voltage vector optimizing-combination algorithm [5], [6] and the band-stop filter [2] are introduced to current loop. Besides, the low-order current harmonic components become controllable through the proportional-resonant current controller [7], [8] and proportional-integral (PI) current controller (in multiple reference frame) [9], leading to the suppressed torque ripple.

Although the current harmonics are suppressed in above-mentioned research work, the current dynamic character is not studied. To further optimize the current dynamic character, the bandwidth of current loop can be increased through the current harmonic compensation [10]. Besides, many current decoupling control methods are proposed in [11] and [12], leading to the improved of the current dynamic performance. On this basis, to further optimize the current dynamic character of FW region, different methods are presented through adjusting the structure of FW closed-loop [13]–[17]. In [13] and [14], the response time of FW loop is reduced by the introduced antiwindup structure. In [15] and [16], the single-current-loop structure is applied for current decoupling control in FW region. In [17], the scalar and vector control structures are combined for robust and dynamic improvement. However, the methods in [13]–[17] focus on the influence of the system-structure to current dynamic control, but the current dynamic character that is reflected in MTO trajectory is not analyzed. To solve this problem, the relation between current dynamic control and voltage margin requirement in FW region is analyzed qualitatively in [18]. On this basis, the voltage compensation-based method [18] and the voltage reservation-based method [19], [20] are adopted to satisfy the voltage margin requirement of FW control. Nevertheless, since the accurate dynamic model of MTO trajectory is not presented, the voltage margin requirement cannot be quantified. Thus, in FW region, the quantitative relation between the current dynamic control and the voltage margin requirement still need to be revealed. Meanwhile, since MTO trajectory is designed without taking the dynamic current terms into account [1], the specialized current dynamic analysis to MTO trajectory is necessary.

Therefore, this letter proposed quantitative analysis of the current dynamic character in MTO trajectory. The contribution

Manuscript received November 29, 2019; revised January 9, 2020; accepted January 16, 2020. Date of publication January 23, 2020; date of current version May 1, 2020. This work was supported in part by the National Natural Science Foundation of China under Grants 51690182 and 51807038, in part by the China Postdoctoral Science Foundation Funded Project under Grants 2018M630354 and 2019T120267, in part by the Heilongjiang Postdoctoral Foundation Funded Project under Grant LBH-Z18097, and in part by the Fundamental Research Funds for the Central Universities (HIT.NSRIF.2019025). *(Corresponding author: Yong Yu.)*

The authors are with the School of Electrical Engineering and Automation, Harbin Institute of Technology, Harbin 150001, China (e-mail: zhangxu_hitee@163.com; wangbohit@hit.edu.cn; yuyong@hit.edu.cn; zhangjing_hitee@163.com; hitpeeddjx@163.com; xudiang@ hit.edu.cn).

Color versions of one or more of the figures in this article are available online at https://ieeexplore.ieee.org.

Digital Object Identifier 10.1109/TPEL.2020.2968978

of this letter is to calculate the current changing rate and voltage margin requirement as the current vector moves along MTO trajectory under different load. On this basis, the *d*-axis voltage margin priority method is applied to the IM FW system to optimize the current dynamic performance.

This letter is arranged as follows. In Section II, the MTO trajectory is given. In Section III, the current changing rate and voltage margin requirement of MTO trajectory are calculated and graphically represented. Section IV shows the *d*-axis voltage margin priority-combined IM FW system. Finally, the studied method is experimentally evaluated in Section V.

II. MTO Trajectory in IM FW Region

To achieve current dynamic analysis, this section first gives the MTO trajectory of FW region. In the rotor field-oriented control (RFOC) based IM control system, the IM voltage equations of synchronous rotating frame can be expressed as [21]:

$$\begin{cases} u_{sd} = R_s i_{sd} - \omega_e \sigma L_s i_{sq} + \sigma L_s p i_{sd} + \frac{L_m}{L_r} p\lambda_r \\ u_{sq} = R_s i_{sq} + \omega_e \sigma L_s i_{sd} + \sigma L_s p i_{sq} + \omega_e \frac{L_m}{L_r} \lambda_r \end{cases} \tag{1}$$

where $u_{sd,q}$ is the *d, q*-axis stator voltages; $i_{sd,q}$ is the *d,q*-axis stator currents; L_s, L_r, and L_m are stator self-inductance, rotor self-inductance, and mutual inductance, respectively; $\sigma = 1 - L2\,m/(L_s L_r)$ is the leakage factor; ω_e is the synchronous frequency. R_s is the stator resistance; λ_r is the rotor flux; and *p* is the differential operator.

By neglecting the stator resistance and the dynamic terms of (1), the steady-state IM voltage equations of FW region can be expressed as [1]

$$u_{sd} = -\omega_e \sigma L_s i_{sq} \tag{2a}$$

$$u_{sq} = \omega_e L_s i_{sd}. \tag{2b}$$

In FW region I, the maximum voltage (u_{smax}) and maximum current (i_{smax}) are employed for maximum torque output

$$i_{sd}^2 + i_{sq}^2 = i_{\mathrm{smax}}^2 \tag{3a}$$

$$u_{sd}^2 + u_{sq}^2 = u_{\mathrm{smax}}^2. \tag{3b}$$

In FW region II, to maintain the maximum slip frequency constraint, i_{sd} and i_{sq} satisfy the following relation:

$$i_{sq} = i_{sd}/\sigma. \tag{4}$$

Fig. 1 shows the MTO trajectory according to (2)–(4). In FW region I, the current vector moves along arc CD, while the voltage vector moves along arc AB. Arcs AB and CD are on the voltage and current constraint circles, respectively. In FW region II, current vector moves along line DO, while voltage vector stays at point B. The slope of line OD is $1/\sigma$.

The output torque of MTO trajectory can be expressed as [1]

$$T_e = \frac{3 n_p L_m^2 i_{sq} i_{sd}}{2 L_r} \tag{5}$$

where n_p is the number of pole-pairs.

According to (5), the constant torque curves are hyperbolics in $i_{sd} - i_{sq}$ frame, as shown in Fig. 1 (the green lines). T_{e1}, T_{e2}, and T_{e3} $(T_{e3} < T_{e2} < T_{e1})$ are the corresponding output torque

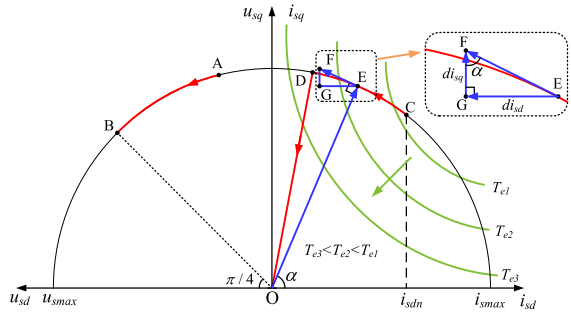

Fig. 1. MTO trajectory in FW region.

of the constant torque curves. During the current vector moves along the MTO trajectory, the constant torque curve in which the current vector is located approaches to the coordinate axis gradually. Accordingly, the output torque will decrease with the decreasing i_{sd} in FW region.

III. Proposed Quantitative Analysis of Current Dynamic Character in FW Region

In this section, the current changing rate is calculated as the current vector moves along MTO trajectory under different load torque. On this basis, the changing law of the current dynamic rate and voltage margin requirement is summarized.

A. Calculation of Current Changing Rate in MTO Trajectory

It can be seen in (1) that there are five unknown quantities under the certain stator voltage and speed. They are i_{sd}, i_{sq}, pi_{sd}, pi_{sq}, and $p\lambda_r$. The current changing rate cannot be calculated with only the two equations in (1). Therefore, the original voltage equation is fail to calculate the current changing rate of FW region.

To solve this problem, this letter neglected the transient voltage terms in (1), and then, calculated the current changing rate through the derivative functions of the steady-state voltage equations in (2). It is feasible to neglect the transient voltage terms for the current changing rate calculation in FW region. The corresponding proof is given in the Appendix.

The changing rate of i_{sd} can be obtained by the derivative function of (2b)

$$\frac{di_{sd}}{dt} = \frac{1}{L_s \omega_e} \cdot \frac{du_{sq}}{dt} - \frac{i_{sd}}{\omega_e} \cdot \frac{d\omega_e}{dt} \tag{6}$$

where *d* is the differential operator.

In (6), to calculate di_{sd}/dt, the values of i_{sd}, ω_e, $d\omega_e/dt$, and du_{sq}/dt need to be calculated in advance. To facilitate these four intermediate variables calculation, a coefficient F_D is introduced to show FW degree. F_D is expressed as

$$F_D = (i_{sdn} - i_{sd})/i_{sdn} \tag{7}$$

where i_{sdn} is the rated field current.

It can be seen that F_D increases with the decreasing i_{sd}. FW region I is corresponding to $0 < F_D < (i_{sdn} - i_{sdc})/i_{sdn}$, while FW region II is corresponding to $(i_{sdn} - i_{sdc})/i_{sd} \leq F_D < 1$. $i_{sdc} = \sigma^* i_{\mathrm{smax}}/(1+\sigma^2)^{1/2}$ is the field current at the

critical point between FW regions I and II. Based on the introduced F_D, the four intermediate variables i_{sd}, ω_e, $d\omega_e/dt$, and du_{sq}/dt in (6) can be calculated through the following four steps.

Step one: According to (3a), (4), and (7), i_{sd} and i_{sq} can be expressed as functions of F_D

$$\begin{cases} i_{sd} = (1-F_D)\, i_{sdn} \\ i_{sq} = \begin{cases} \sqrt{i_{s\max}^2 - \left[(1-F_D)\, i_{sdn}\right]^2} & (\text{FW region I}) \\ (1-F_D)\, i_{sdn}/\sigma & (\text{FW region II}). \end{cases} \end{cases} \tag{8}$$

Step two: According to (2) and (3b), ω_e can be expressed as

$$\omega_e = u_{s\max}/\sqrt{\left(L_s i_{sd}\right)^2 + \left(\sigma L_s i_{sq}\right)^2}. \tag{9}$$

By substituting (8) into (9), ω_e can be calculated with F_D.

Step three: $d\omega_e/dt$ can be expressed as

$$\frac{d\omega_e}{dt} = \frac{n_p}{J}\left(\frac{1.5 n_p L_m^2 i_{sd} i_{sq}}{L_r} - T_L\right) + \frac{d\omega_s}{dt} \tag{10}$$

where *J* is the motor rotational inertia; T_L is the load torque; n_p is the pole-pairs number; L_m and L_r are the mutual inductance and rotor inductance; and ω_s is slip frequency.

In (10), $d\omega_s/dt$ needs to be further calculated. In FW region II, since ω_s keeps at the maximum value, $d\omega_s/dt$ is zero. In FW region I, $d\omega_s/dt$ can be expressed as

$$\frac{d\omega_s}{dt} = \frac{d\left(i_{sq}/i_{sd}\right)}{T_r dt} = \frac{d\left(\tan\alpha\right)}{T_r dt} = \frac{1}{T_r \cos^2\alpha}\frac{d\alpha}{d\omega_e}\frac{d\omega_e}{dt} \tag{11}$$

where $T_r = L_r/R_r$ (R_r is the rotor resistance) is the rotor time-constant; α is the angle between the current vector and the *d*-axis (see Fig. 1: α is the angle between OE and *d*-axis).

In (11), $d\alpha/d\omega_e$ is unknown. Here, an equation of i_{sd} is given to calculate $d\alpha/d\omega_e$

$$\begin{aligned} i_{s\max}\cos\alpha &= i_{sd} \\ &= \sqrt{\left[u_{s\max}^2 - \left(\omega_e \sigma L_s i_{s\max}\right)^2\right] / \left[\left(1-\sigma^2\right)\left(\omega_e L_s\right)^2\right]} \end{aligned} \tag{12}$$

where the right-hand-side formula can be obtained by substituting (2) and (3a) into (3b).

Equation (12) can be transformed into

$$\begin{aligned} M\left(\omega_e\right) &= \left(\frac{u_{s\max}}{\omega_e L_s}\right)^2 - \left(\sigma i_{s\max}\right)^2 \\ &= i_{s\max}^2 \cos^2\alpha\left(1-\sigma^2\right) = N\left(\alpha\right) \end{aligned} \tag{13}$$

where $M(\omega_e)$ and $N(\alpha)$ are the intermediate functions for ease of $d\alpha/d\omega_e$ calculation.

According to (13), $d\alpha/d\omega_e$ can be calculated as

$$\begin{cases} \frac{d\alpha}{d\omega_e} = \frac{dM(\omega_e)/d\omega_e}{dN(\alpha)/d\alpha} = \frac{\left(u_{s\max}/L_s\right)^2 \omega_e^{-3}}{i_{s\max}^2\left(1-\sigma^2\right)\cos\alpha\sin\alpha} \\ \cos\alpha = i_{sd}/i_{s\max}, \quad \sin\alpha = i_{sq}/i_{s\max}. \end{cases} \tag{14}$$

Then, (10) and (11) can constitute a binary equation system of $d\omega_e/dt$ and $d\omega_s/dt$ by substituting (14) into (11). On this basis, $d\omega_e/dt$ can be calculated with certain F_D and T_L.

Step four: With respect to du_{sq}/dt calculation, du_{sq}/dt is equal to zero in FW region II due to the invariable u_{sq}. As for FW region I, u_{sq} can be calculated by substituting (2b) and (3a) into (3b)

$$u_{sq}^2 = \frac{u_{s\max}^2 - \left(\omega_e \sigma L_s i_{s\max}\right)^2}{1-\sigma^2}. \tag{15}$$

du_{sq}/dt can be obtained by the derivative function of (15)

$$\begin{aligned} \frac{du_{sq}}{dt} &= -\frac{1}{u_{sq}}\frac{\omega_e\left(\sigma L_s i_{s\max}\right)^2}{1-\sigma^2}\frac{d\omega_e}{dt} \\ &= -\frac{1}{L_s i_{sd}}\frac{\left(\sigma L_s i_{s\max}\right)^2}{1-\sigma^2}\frac{d\omega_e}{dt}. \end{aligned} \tag{16}$$

In (16), since i_{sd} and $d\omega_e/dt$ are functions of F_D and T_L, du_{sq}/dt is also a function of F_D and T_L.

Finally, by substituting the calculated i_{sd}, ω_e, $d\omega_e/dt$, and du_{sq}/dt into (6), di_{sd}/dt of FW regions I and II can be calculated with certain F_D and T_L.

Moreover, di_{sq}/dt can be calculated according to di_{sd}/dt. In FW region I, di_{sq}/dt is calculated as follows: as shown in Fig. 1, OE is the current vector; EF is the instantaneous change of OE, which is tangent to arc CD. EF is further shown in the enlarged view. EG and GF are the *d,q*-axis components of EF. The angle between EF and GF is equal to α. Thus, di_{sq}/dt can be calculated in right triangle EFG

$$\begin{cases} \frac{di_{sq}}{dt} = \frac{di_{sq}}{|di_{sd}|}\cdot\frac{|di_{sd}|}{dt} = -\frac{1}{\tan\alpha}\cdot\frac{di_{sd}}{dt} \\ \alpha = \arccos\left((1-F_D)\, i_{sdn}/i_{s\max}\right). \end{cases} \tag{17}$$

In FW region II, di_{sq}/dt can be calculated by di_{sd}/dt according to the derivative function of (4)

$$\frac{di_{sq}}{dt} = \frac{di_{sd}}{dt}\cdot\frac{1}{\sigma}. \tag{18}$$

By substituting the calculation results of di_{sd}/dt into (17) and (18), di_{sq}/dt of FW regions I and II can be obtained.

B. Analysis of Current Changing Rate and Voltage Margin Requirement in MTO Trajectory

According to the IM parameters (see Section V), $di_{sd(q)}/dt$ in MTO trajectory can be calculated through (6)–(18). In addition to $di_{sd(q)}/dt$, the voltage margin requirement $(u_{sd(q),\text{req}})$ for current dynamic control can be calculated by: $u_{sd,\text{req}} = L_s di_{sd}/dt$ and $u_{sq,\text{req}} = \sigma L_s di_{sq}/dt$.

Fig. 2 shows the calculation results of di_{sq}/dt, di_{sd}/dt, and $u_{sd(q),\text{req}}$ with variation of F_D and T_L. In Fig. 2(a) and (b), it can be seen that di_{sq}/dt is greater than 0 in FW region I and less than 0 in FW region II, while di_{sd}/dt is less than 0 in the whole FW region. The minimum and maximum di_{sq}/dt are -6 A/s and 4.78 A/s, respectively, while the minimum di_{sd}/dt is -12.83 A/s. Under the invariable T_L, both $|di_{sq}/dt|$ and $|di_{sd}/dt|$ decrease with the increasing F_D in FW regions I and II. di_{sd}/dt and di_{sq}/dt do not change continuously at

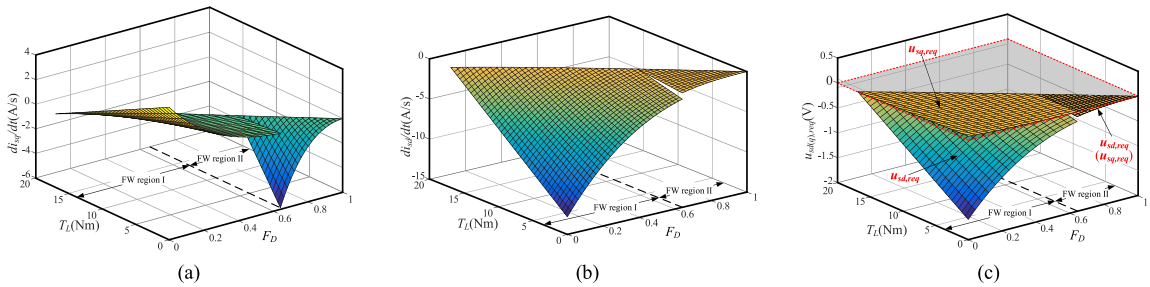

Fig. 2. Current changing rate and voltage margin requirement in MTO trajectory with variation of F_D and T_L. (a) di_{sq}/dt. (b) di_{sd}/dt. (c) $u_{sd(q),\mathrm{req}}$.

the critical point between FW regions I and II. Taking $T_L = 0$ condition as an example, when entering FW region II, di_{sq}/dt decreases by 6.12 A/s, while di_{sd}/dt increases by 0.74 A/s. Under the invariable F_D, both $|di_{sq}/dt|$ and $|di_{sd}/dt|$ decrease with the increasing T_L. When T_L increases to the maximum load, $|di_{sd(q)}/dt|$ decreases to 0.

As for $u_{sd(q),\mathrm{req}}$ in Fig. 2(c), in FW region I, $u_{sq,\mathrm{req}}$ is greater than 0, while $u_{sd,\mathrm{req}}$ is less than 0. $|u_{sd,\mathrm{req}}|$ is much bigger than $u_{sq,\mathrm{req}}$. Taking $T_L = 0$ and $F_D = 0$ condition as an example, $|u_{sd,\mathrm{req}}|$ is about 23 × that of $u_{sq,\mathrm{req}}$ ($|u_{sd,\mathrm{req}}| = 1.59$ V, $u_{sq,\mathrm{req}}$ = 0.07 V). $u_{sd(q),\mathrm{req}}$ does not change continuously at the critical point between FW regions I and II. In FW region II, $u_{sq,\mathrm{req}}$ is equal to $u_{sd,\mathrm{req}}$, both $|u_{sq,\mathrm{req}}|$ and $|u_{sd,\mathrm{req}}|$ are very small ($-0.08\mathrm{V} < u_{sd(q),\mathrm{req}} < 0$). Taking the whole FW region into consideration, under the invariable T_L, $|u_{sd(q),\mathrm{req}}|$ decreases with the increasing F_D. Under the invariable F_D, $|u_{sd(q),\mathrm{req}}|$ decreases with the increasing T_L.

From Fig. 2, the following conclusions can be drawn about the current dynamic control in FW region.

1) Under voltage limitation condition, since $|u_{sd(q),\mathrm{req}}|$ and $|di_{sd(q)}/dt|$ decrease with the increasing F_D, the current dynamic control can be easier to realize in deep FW degree than shallow FW degree.
2) Since $|u_{sd(q),\mathrm{req}}|$ and $|di_{sd(q)}/dt|$ decrease with the increasing T_L, the current dynamic control can be easier to realize with heavy load than light load in FW region.
3) Since $u_{sd,\mathrm{req}}$ is much bigger than $u_{sq,\mathrm{req}}$ in FW region I, the *d*-axis voltage margin priority should be provided for current dynamic control.

IV. *d*-Axis Voltage Margin Priority Method for Current Dynamic Optimization

In this section, according to the conclusion in (3), in Section III, the *d*-axis voltage margin priority method is designed to optimize the current dynamic performance in FW region.

As shown in Fig. 3, the *d*-axis voltage priority module is introduced to the voltage closed-loop-based IM FW system. The two voltage regulators work for MTO trajectory realization. If the feedback voltage amplitude (u_{fdb}) exceeds $u_{\max}$ in FW region I, i_{sd} will be weakened by voltage regulator 1 to pull back the exceeded voltage. Then, i_{sq} and $|u_{sd}|$ will increase with the decreasing i_{sd}. When $|u_{sd}|$ exceeds $0.707u_{\mathrm{smax}}$, FW region II begins, and i_{sq} will be weakened by voltage regulator 2 to control $|u_{sd}| = 0.707u_{\mathrm{smax}}$.

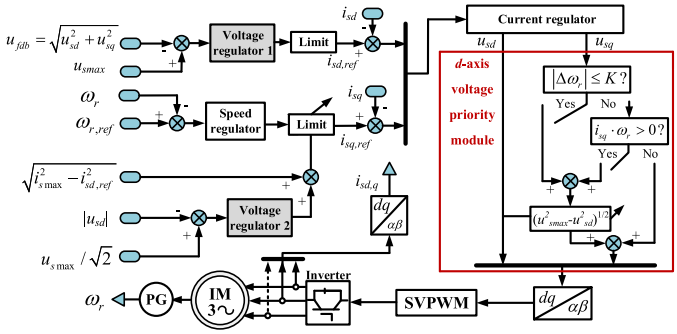

Fig. 3. *d*-axis voltage priority method-combined IM FW control system.

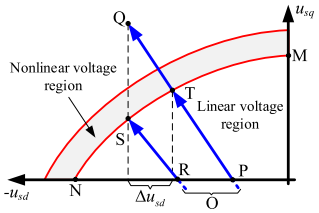

Fig. 4. Working process of *d*-axis voltage priority structure.

In the *d*-axis voltage priority module of Fig. 3, the limitation value of the *q*-axis voltage is set to $(u_{\mathrm{smax}}^2 - u_{sd}^2)^{1/2}$ in steady state and acceleration process. The steady state is judged by $|\Delta\omega_r| \le K$, where $\Delta\omega_r$ is the speed following error, and *K* is a constant value chosen artificially; the acceleration process is judged by $i_{sq}{}^*\omega_r > 0$.

Fig. 4 shows the realization process of the *d*-axis voltage margin priority in *d*–*q* frame. Arc MN is voltage constraint circle. The shadow region is nonlinear voltage region. Point O is the ordinate origin that is on the extension cord of QP and SR. PQ is a voltage vector in FW region. In a conventional method, PQ will be limited to PT by inverter; in the *d*-axis voltage priority method, PQ will be limited to RS by the *q*-axis voltage limitation. The *d*-axis voltage margin of RS is increased by Δu_{sd} over PT. In this way, the *d*-axis voltage margin priority is implemented. Besides, since the voltage vector cannot extend out of arc MN, the nonlinear voltage region can be eliminated in the *d*-axis voltage priority method.

In the FW system of Fig. 3, the two voltage regulators are both PI type controller. Since the field current reference are obtained through the PI voltage controller instead of through

the machine model, the parameter uncertainty or nonlinearity will not influence the current control from the reference side. Accordingly, the voltage closed-loop-based FW control system has high robustness to machine parameter uncertainty or nonlinearity [1]. Meanwhile, the introduced d-axis voltage priority module does not influence the system high robustness. The d-axis voltage priority module only works in steady state and acceleration process. The steady state and acceleration process are judged through the feedback current and feedback speed, which are detected by sampling resistor and encoder directly. On one hand, the judging of the IM operation state cannot be affected by machine parameter uncertainty or nonlinearity. On the other hand, since the voltage vector is adjusted only according to the voltage constraint circle when the d-axis voltage priority module acts, the parameter uncertainty and nonlinearity will not influence the effectiveness of the proposed method.

Therefore, the parameter uncertainty and nonlinearity will not influence the current control through impacting the voltage loop structure and the d-axis voltage priority module. However, the calculation of decoupling voltage terms and the compensation of back EMF in current regulator are based on the accurate motor parameters. Meanwhile, since IM is the controlled object of current loop, the parameter nonlinearity can influence the bandwidth of the current loop. Therefore, the parameter uncertainty or nonlinearity would deteriorate the current control through impacting the current regulator and the current-loop bandwidth. Since this is the inherent problem in vector control and many research works are presented to deal with this problem [17], [22], [23], this letter will not focus on this problem.

V. Experimental Results

The d-axis voltage priority method-combined IM FW system is realized on an STM32F103 advanced RISC machine (ARM)-based experimental platform. The space vector pulsewidth modulation (SVPWM) switching frequency is 8 kHz. Two same IMs are applied in the platform, which are used for algorithm testing and load providing, respectively.

The IM parameters are as follows. The rated power is 3.7 kW; the base speed is 1500 r/min; $u_{\mathrm{smax}} = 380$ V; $i_{\mathrm{smax}} = 8.9$ A; $R_s = 1.142\ \Omega$; $R_r = 0.825\ \Omega$; $L_m = 0.1189$ H; and $L_s = L_r = 0.1244$ H. The coefficients of the PI regulators are as follows: the current loop is $K_{pc} = 10$, $K_{ic} = 0.5$; the speed loop is $K_{ps} = 3$, $K_{is} = 55$; and the voltage loop is $K_{pv} = 0.05$, $K_{iv} = 0.5$.

Fig. 5 shows the comparison results of step acceleration process in the conventional method and proposed method. In the conventional method of Fig. 5(a), $i_{sd(q),\mathrm{ref}}$, $i_{sd(q),fdb}$, and T_e keep at the rated value in base-speed region. Then, $i_{sd,fdb}$ decreases gradually in FW region, while $i_{sq,fdb}$ increases with the decreasing $i_{sd,fdb}$. In addition, T_e begins to decrease with the decreasing $i_{sd,fdb}$. It can be seen that the current ripple and torque ripple of 0.28–0.44 s is more serious than 0.44–0.80 s. Thus, the current dynamic control is easy to realize in deep FW-degree region, which is consistent with conclusion (1) of Section III.

In the proposed method of Fig. 5(b), the waveforms are same with Fig. 5(a) in base-speed region. In FW region, it can be seen

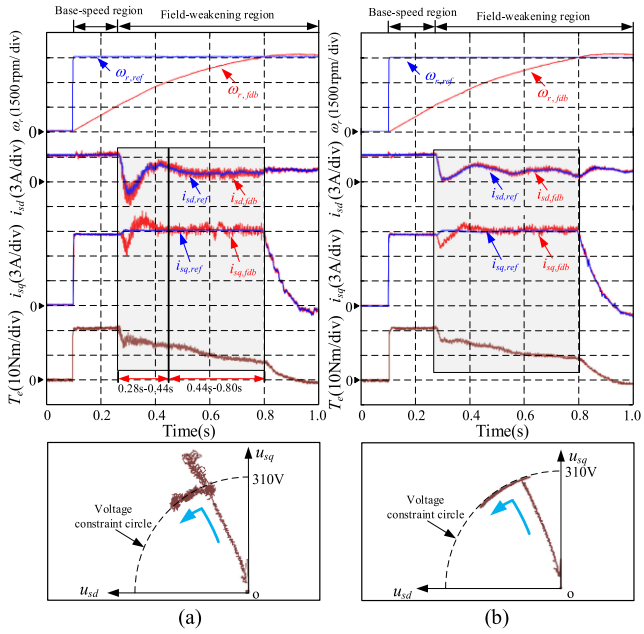

Fig. 5. Step acceleration process from 0 to 4500 r/min (3p.u.). From top to bottom: reference and feedback values of field current ($i_{sd,\mathrm{ref}}$ and $i_{sd,fdb}$); reference and feedback values of torque current ($i_{sq,\mathrm{ref}}$ and $i_{sq,fdb}$); and voltage trajectory. (a) Conventional method. (b) Proposed method.

that the exceeded voltage is limited to the constraint circle by the q-axis voltage limitation. Consequently, with the d-axis voltage margin priority, it can be seen that the current dynamic performance of shadow box is better than the conventional method, which is consistent with the conclusion in (3) of Section III. Meanwhile, the optimized current dynamic control leads to the reduced torque ripple of FW region.

For more comprehensive evaluations, the conventional method and the proposed method are further compared under the speed reference piecewise changes. As shown in Fig. 6, the speed reference step changes from 0 to 1500 r/min at 0.25 s, and then step changes from 1500 to 3000 r/min at 1.00 s, finally step changes from 3000 to 4500 r/min at 1.75 s. In the conventional method of Fig. 6(a), when speed reference step changes from 0 to 1500 r/min, since the IM does not enter the FW region, there are no ripples in current and torque waveforms. Then, during the acceleration process from 1500 to 3000 r/min and from 3000 to 4500 r/min, the tracking performance of current is deteriorated, and the torque ripple appears. Meanwhile, the output torque decreases with the increasing speed. Accordingly, the acceleration time of feedback speed is extended gradually. It can be seen that the acceleration times of the three acceleration processes of Fig. 6(a) are 0.168 s, 0.198 s, and 0.375 s, respectively.

In the proposed method of Fig. 6(b), the current tracking performance is better than conventional method during the acceleration process from 1500 to 3000 r/min and 3000 to 4500 r/min. Besides, the output torque ripple is reduced. The acceleration times are 0.168 s, 0.196 s, and 0.378 s, respectively, which are approximately equal to the conventional method.

Fig. 7 shows the output torque, phase current, and phase current spectrum at 4500 r/min (3 p.u.) under different load in the conventional method and proposed method. The load

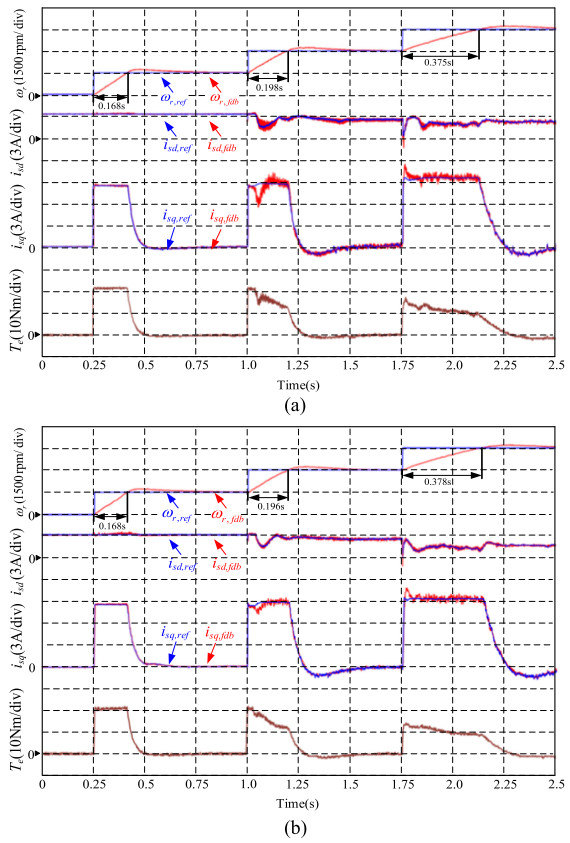

Fig. 6. Experimental results under speed reference piecewise changes. From top to bottom: reference and feedback values of rotor speed ($\omega_{r,\mathrm{ref}}$ and $\omega_{r,fdb}$); reference and feedback values of field current ($i_{sd,\mathrm{ref}}$ and $i_{sd,fdb}$); reference and feedback values of torque current ($i_{sq,\mathrm{ref}}$ and $i_{sq,fdb}$); and output torque (T_e). (a) Conventional method. (b) Proposed method.

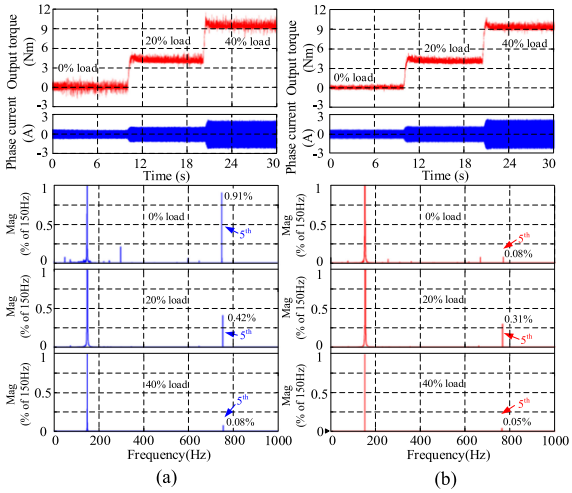

Fig. 7. Waveforms of output torque, phase current, and phase current spectrum at 4500 r/min (3 p.u.) under 0%, 20%, and 40% rated load. (a) Conventional method. (b) Proposed method.

torque increases by 20% rated value every 10 s. It can be seen that the torque ripple of the proposed method is smaller than conventional method. Moreover, in the conventional method, the proportion of fifth-phase current harmonics are 0.91%, 0.42%, and 0.08% under 0%, 20%, and 40% rated load, respectively. By contrast in the proposed method, the fifth current harmonics are reduced to 0.08%, 0.31%, and 0.05%. Thus, since the nonlinear voltage is eliminated in the proposed method, the torque ripple and current harmonics of FW region is suppressed.

V. Conclusion

This letter proposed quantitative analysis of the current dynamic character in IM FW control. The current changing rate and the voltage margin requirement are proved to decrease with the increasing load torque and the deepening FW degree during the current vector moving along MTO trajectory. It means that the current dynamic control is easy to realize in heavy load and deep FW degree. Moreover, it is confirmed that dozens of times more voltage margin is needed in the d-axis than the q-axis to control the current vector move along MTO trajectory in FW region. On this basis, the d-axis voltage margin priority is realized in acceleration process and steady state. The experimental results verify the analysis-correctness and show that the d-axis voltage priority method can optimize current dynamic and reduce torque ripple in FW region.

Appendix

It is feasible to neglect the transient voltage terms for the current changing rate calculation in FW region. The corresponding proof is given as follows.

In the RFOC-based IM control system, the rotor flux can be expressed as [24]:

$$\lambda_r = \frac{L_m}{\frac{L_r}{R_r}p+1}\cdot i_{sd}. \tag{19}$$

$L_m/(pL_r/R_r+1)$ of (19) can be regarded as a low-pass filter. In synchronous rotating frame, since i_{sd} is mainly composed of low-frequency components, the low-pass filter can be approximated as a proportional link. Then, (19) can be transformed into $\lambda_r = L_m i_{sd}$.

By substituting $\lambda_r = L_m i_{sd}$ to (1) and neglecting the stator resistance terms, (1) can be rewritten as

$$\begin{cases} u_{sd} = -\omega_e \sigma L_s i_{sq} + L_s di_{sd}/dt \\ u_{sq} = \omega_e L_s i_{sd} + \sigma L_s di_{sq}/dt. \end{cases} \tag{20}$$

To eliminate the differential terms, (20) can be transformed into

$$\begin{cases} u_{sd} + \omega_e \int_{t_0}^{t_0+t} u_{sq}dt = \omega_e L_s \int_{t_0}^{t_0+t} \omega_e i_{sd}dt + L_s di_{sd}/dt \\ u_{sq} - \omega_e \int_{t_0}^{t_0+t} u_{sd}dt = \omega_e \sigma L_s \int_{t_0}^{t_0+t} \omega_e i_{sq}dt + \sigma L_s di_{sq}/dt \end{cases} \tag{21}$$

where t_0 is the initial time of integral.

Assuming that the speed increase in t period of time is $\Delta\omega_e(t)$ and the initial speed is ω_{e0}. Then, (21) can be transformed into

$$\begin{cases} u_{sd} + \omega_e \int_{t_0}^{t_0+t} u_{sq}dt = \omega_e L_s \int_{t_0}^{t_0+t} (\omega_{e0} + \Delta\omega_e(t)) i_{sd}dt \\ \quad + L_s di_{sd}/dt \\ u_{sq} - \omega_e \int_{t_0}^{t_0+t} u_{sd}dt = \omega_e \sigma L_s \int_{t_0}^{t_0+t} (\omega_{e0} + \Delta\omega_e(t)) i_{sq}dt \\ \quad + \sigma L_s di_{sq}/dt. \end{cases} \tag{22}$$

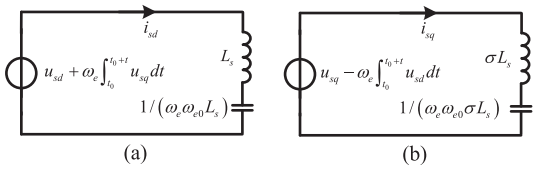

Fig. 8. Equivalent circuit diagram of (23).

Since ω_{e0} is bigger than the rated speed in FW region, $\Delta\omega_e(t)$ of (22) is much less than ω_{e0} when t is small. Therefore, (22) can be transformed into (23) by neglecting $\Delta\omega_e(t)$

$$\begin{cases} u_{sd}+\omega_e\int_{t_0}^{t_0+t}u_{sq}dt=\omega_e L_s\omega_{e0}\int_{t_0}^{t_0+t}i_{sd}dt+L_s di_{sd}/dt \\ u_{sq}-\omega_e\int_{t_0}^{t_0+t}u_{sd}dt=\omega_e\sigma L_s\omega_{e0}\int_{t_0}^{t_0+t}i_{sq}dt+\sigma L_s di_{sq}/dt. \end{cases} \tag{23}$$

According to the characteristics of (23), the left-hand side of (23) can be regarded as voltage sources, while the integral and differential terms on the right-hand side of (23) can be regarded as the terminal voltage of capacitance and inductance. Therefore, (23) can be represented by the two equivalent circuits, as shown in Fig. 8.

In Fig. 8(a), the complex impedance of the inductance and capacitance is

$$z=j\omega_{i_{sd}}\left(L_s-\frac{\omega_e\omega_{e0}}{\omega_{i_{sd}}^2}L_s\right) \tag{24}$$

where z is the complex impedance; j is the imaginary unit; and ω_{isd} is the frequency of i_{sd}.

In Fig. 8(b), the complex impedance of the inductance and capacitance is

$$z=j\omega_{i_{sq}}\sigma\left(L_s-\frac{\omega_e\omega_{e0}}{\omega_{i_{sq}}^2}L_s\right) \tag{25}$$

where ω_{isq} is the frequency of i_{sq}.

In (24) and (25), ω_e and ω_{e0} are higher than rated speed in FW region. Meanwhile, after rotation transformation, the stator currents become dc variables and mainly composed of low-frequency components. Therefore, ω_{isd} and ω_{isq} are much smaller than ω_e and ω_{e0}. The proportion of inductance terms in complex impedance is much smaller than capacitance term in (24) and (25). Accordingly, the influence of inductance on current changes can be neglected in Fig. 8. Since the inductances in Fig. 8 are corresponding to the transient voltage terms of (1), the transient terms can be neglected for the current dynamic analysis in FW region. Therefore, it is feasible to neglect the transient voltage terms for the current changing rate calculation in FW region.

REFERENCES

[1] S. H. Kim and S. K. Sul, "Voltage control strategy for maximum torque operation of an induction machine in the field-weakening region," *IEEE Trans. Ind. Electron.*, vol. 44, no. 4, pp. 512–518, Aug. 1997.

[2] B. Wang, X. Zhang, Y. Yu, J. Zhang, and D. Xu, "Maximum torque analysis and extension in six-step mode-combined FW control for induction motor drives," *IEEE Trans. Ind. Electron.*, vol. 66, no. 12, pp. 9129–9138, Dec. 2019.

[3] H. Y. O. Yang and R. D. Lorenz, "Torque ripple minimization in six-step PMSM drives via variable and fast DC bus dynamics," *IEEE Trans. Ind. Appl.*, vol. 55, no. 4, pp. 3791–3802, Jul./Aug. 2019.

[4] I.Ralev, T. Lange, and R.W. D. Doncker, "Wide speed range six-step mode operation of IPMSM drives with adjustable dc-link voltage," in *Proc. IEEE Int. Conf. Elect. Mach. Syst.*, Hangzhou, China, 2014, pp. 2987–2993.

[5] K. Nishizawa, J. Itoh, A. Odaka, A. Toba, and H. Umida, "Current harmonic reduction based on space vector PWM for DC-link capacitors in three-phase VSIs operating over a wide range of power factor," *IEEE Trans. Power Electron.*, vol. 34, no. 5, pp. 4853–4867, May 2019.

[6] J. Hobraiche, J.-P. Vilain, P. Macret, and N. Patin, "A new PWM strategy to reduce the inverter input current ripples," *IEEE Trans. Power Electron.*, vol. 24, no. 1, pp. 172–180, Jan. 2009.

[7] J. Gao, X.Wu, S. Huang, W. Zhang, and L. Xiao, "Torque ripple minimization of permanent magnet synchronous motor using a new proportional resonant controller," *IET Power Electron*., vol. 10, no. 2, pp. 208–214, Oct. 2017.

[8] C. Xia, B. Ji, and Y. Yan, "Smooth speed control for low-speed high-torque permanent-magnet synchronous motor using proportional-integral-resonant controller," *IEEE Trans. Ind. Electron.*, vol. 62, no. 4, pp. 2123–2134, Apr. 2015.

[9] G. Feng, C. Lai, J. Tian, and N. C. Kar, "Multiple reference frame based torque ripple minimization for PMSM drive under both steady-state and transient conditions," *IEEE Trans. Power Electron.*, vol. 34, no. 7, pp. 6685–6696, Jul. 2009.

[10] A. M. Khambadkone and J. Holtz, "Compensated synchronous PI current controller in overmodulation range and six-step operation of space-vector-modulation-based vector-controlled drives," *IEEE Trans. Ind. Electron.*, vol. 49, no. 3, pp. 574–580, Jun. 2002.

[11] K. Lee, J. I. Ha, and D. V. Simili, "Analysis and suppression of slotting and cross-coupling effects on current control in PM synchronous motor drives," *IEEE Trans. Power Electron.*, vol. 34, no. 10, pp. 9942–9956, Oct. 2019.

[12] M. Comanescu, L. Xu, and T. D. Batzel, "Decoupled current control of sensorless induction-motor drives by integral sliding mode," *IEEE Trans. Ind. Electron.*, vol. 55, no. 11, pp. 3836–3845, Nov. 2008.

[13] W. Xu, M. M. Ismail, Y. Liu, and M. R. Islam, "Parameter optimization of adaptive flux-weakening strategy for permanent-magnet synchronous motor drives based on particle swarm algorithm," *IEEE Trans. Power Electron.*, vol. 34, no. 12, pp. 12128–12140, Dec. 2019.

[14] S. K. Sahoo and T. Bhattacharya, "Field weakening strategy for a vector-controlled induction motor drive near the six-step mode of operation," *IEEE Trans. Power Electron.*, vol. 31, no. 4, pp. 3043–3051, Apr. 2016.

[15] J. Park, S. Jung, and J.-I. Ha, "Variable time step control for six-step operation in surface-mounted permanent magnet machine drives," *IEEE Trans. Power Electron.*, vol. 33, no. 2, pp. 1501–1513, Feb. 2018.

[16] Z. Zhang, C. Wang, M. Zhou, and X. You, "Flux-weakening in PMSM drives: Analysis of voltage angle control and the single current controller design," *IEEE J. Emerg. Sel. Topics Power Electron.*, vol. 7, no. 1, pp. 437–445, Mar. 2019.

[17] S. R. P. Reddy and U. Loganathan, "Robust and high-dynamic-performance control of induction motor drive using transient vector estimator," *IEEE Trans. Ind. Electron.*, vol. 66, no. 10, pp. 7529–7538, Oct. 2019.

[18] Y. C. Kwon, S. Kim, and S. K. Sul, "Six-step operation of PMSM with instantaneous current control," *IEEE Trans. Ind. Appl.*, vol. 50, no. 4, pp. 2614–2625, Jul./Aug. 2014.

[19] M. Mengoni, L. Zarri, A. Tani, G. Serra, and D. Casadei, "A comparison of four robust control schemes for FW operation of induction motors," *IEEE Trans. Power Electron.*, vol. 27, no. 1, pp. 307–320, Jan. 2012.

[20] F. Briz, A. Diez, M. W. Degner, and D. Lorenz, "Current and flux regulation in field-weakening operation," *IEEE Trans. Ind. Appl.*, vol. 37, no. 1, pp. 42–50, Jan./Feb. 2001.

[21] M. Mengoni, L. Zarri, A. Tani, G. Serra, and D. Casadei, "A comparison of four robust control schemes for field-weakening operation of induction motors," *IEEE Trans. Power Electron.*, vol. 27, no. 1, pp. 307–320, Jan. 2012.

[22] J. Kan, K. Zhang, and Z. Wang, "Indirect vector control with simplified rotor resistance adaptation for induction machines," *IET Power Electron.*, vol. 8, no. 7, pp. 1284–1294, 2015.

[23] F. R. Salmasi, T. A. Najafabadi, and P. J. Maralani, "An adaptive flux observer with online estimation of dc-link voltage and rotor resistance for VSI-based inductionmotors," *IEEE Trans. Power Electron.*, vol. 25, no. 5, pp. 1310–1319, May 2010.

[24] S. K. Sul, *Control of Electric Machine Drive Systems*. New York, NY, USA: Wiley, 2011.